Versatile Photonic Entanglement Synthesizer in the Spatial Domain

David Barral,[1,*] Mattia Walschaers,[2] Kamel Bencheikh,[1] Valentina Parigi,[2] Juan Ariel Levenson,[1]
Nicolas Treps,[2] and Nadia Belabas[1,†]

[1] *Centre de Nanosciences et de Nanotechnologies C2N, CNRS, Université Paris-Saclay, 10 boulevard Thomas Gobert, Palaiseau 91120, France*
[2] *Laboratoire Kastler Brossel, Sorbonne Université, CNRS, ENS-PSL Research University, Collège de France, 4 place Jussieu, Paris F-75252, France*

(Received 18 March 2020; revised 30 July 2020; accepted 1 September 2020; published 15 October 2020)

Multimode entanglement is an essential resource for quantum information in continuous-variable systems. Light-based quantum technologies will arguably not be built upon table-top bulk setups, but will presumably rather resort to integrated optics. Sequential bulk opticslike proposals based on cascaded integrated interferometers are not scalable with the current state-of-the-art low-loss materials used for continuous variables. We analyze the multimode continuous-variable entanglement capabilities of a compact currently available integrated bulk-optics analog: the array of nonlinear waveguides. We theoretically demonstrate that this simple and compact structure, together with a reconfigurable input pump distribution and multimode coherent detection of the output modes, is a versatile entanglement synthesizer in the spatial domain. We exhibit this versatility through analytical and numerically optimized multimode squeezing, entanglement, and cluster-state generation in different encodings. Our results re-establish spatial encoding as a contender in the game of continuous-variable quantum information processing.

DOI: 10.1103/PhysRevApplied.14.044025

I. INTRODUCTION

Two key phenomena underpin current quantum technologies [1]: quantum superposition and quantum correlations—entanglement. The paradigmatic example of entanglement is the case of two spatially separated quantum particles that have both maximally correlated momenta and maximally anticorrelated positions [2]. Position and momentum are continuous variables (CVs), i.e., variables that take a continuous spectrum of eigenvalues. In the optical domain, CV-based quantum information can be encoded in the fluctuations of the electromagnetic field quadratures [3]. Features like deterministic resources, unconditional operations, and near-unity efficiency homodyne detectors make CVs a powerful framework for the development of quantum technologies [4]. Remarkably, entanglement between more than two parties is also useful. Large-scale CV entangled states are the resources of a promising class of quantum computing: measurement-based quantum computing (MBQC) [5,6]. A recent breakthrough generating large two-dimensional cylindrical-array clusters positions CVs as a frontrunner in the race after a photonic quantum computer [7,8]. Multipartite entangled states have to date been produced in table-top experiments with specific designs, generating only specific entanglement geometries or quantum networks; recent demonstration of large-scale entanglement include frequency [9], and temporal [10] and spatial [11–13] encoding of squeezed light.

The on-demand generation of different multimode entangled states with the same optical setup—an entanglement synthesizer—is a challenging task. Entanglement synthesizers are key for applications in quantum computing and quantum simulation [14,15]. Transverse laser mode and frequency mode entanglement synthesizers respectively based on postprocessing measurement results and on measurement basis shaping have been introduced in Refs. [16–18]. These supermode-based approaches are interesting for engineering quantum states and simulating complex quantum systems. They are however not fully equivalent to a quantum network, since the quantum information can only be processed locally, but not in a distributed way. Recently, an entanglement synthesizer with the ability to distribute the nodes has been introduced in the time domain [19]. A versatile entanglement synthesizer in the spatial domain is nevertheless still missing. Specifically, spatial distribution of the signal in networks is naturally accomplished in this domain and this is highly desirable for applications in secure communications via quantum secret sharing [20] or in distributed quantum sensing [21]. In this work we introduce the monolithic array of waveguides with built-in nonlinearity

---

[*] david.barral@c2n.upsaclay.fr
[†] nadia.belabas@universite-paris-saclay.fr

as a versatile spatial-mode squeezing and entanglement synthesizer.

We propose to take advantage of integrated optics, a solution for the blooming of market-scalable quantum-optics technologies [22]. Spatial encoding is a natural framework in integrated optics where the information is encoded in the propagating waveguided modes and transmitted by optical fibers. A source of CV entangled states fully on chip has recently been introduced [23]. However, the extension of that scheme of sequential squeezing and entanglement—via nonlinear waveguides and directional couplers, respectively—to a number of modes $N > 2$ is very demanding with current technology. We establish here that the array of nonlinear waveguides (ANWs)—which interlaces nonlinearity and evanescent coupling, i.e., interlaces squeezing and entanglement, in a monolithic way (Fig. 1)—is a good contender for versatile and scalable generation of entanglement. CV entanglement generation in monolithic ANWs is thus paradigmatically different from the current sequential bulk-optics-inspired schemes [11–13]. Nonclassical biphoton states for applications in the discrete-variable (DV) regime have been demonstrated in such waveguide arrays [24,25]. On-chip DV cluster states have recently been demonstrated and proposed in a bulk-optics-inspired scheme and in ANWs [26,27]. Bipartite and tripartite CV entanglement have been predicted in arrays of nonlinear waveguides in the spontaneous parametric down-conversion (SPDC) and stimulated parametric down-conversion regimes [28]. Nevertheless, tripartite entanglement was only predicted there for critical values of the involved parameters. We have recently proposed a scalable approach to generate multipartite entanglement in arrays of nonlinear waveguides in the second harmonic generation regime [29]. We show here that, in the experimentally relevant regime of SPDC, reconfigurable multimode pump and measurement, and the freedom of choice of basis encoding enable on-demand programmability of entanglement. We theoretically demonstrate the versatility of our approach in the production of multimode squeezing, multipartite entanglement, and cluster states, through analytical and numerical solutions, applying optimization strategies. Remarkably, since the encoding of quantum information is mode-basis dependent, we present two cluster-state-generation procedures: (i) entanglement generation among individual modes of the waveguides and (ii) entanglement generation among the elements of optimized nonlocal bases of the array. We thus demonstrate that our photonic entanglement synthesizer can operate in the two regimes pioneered in free-space CVs quantum information processing in (i) [11–13] and (ii) [16–18]. We review the possible applications in each case.

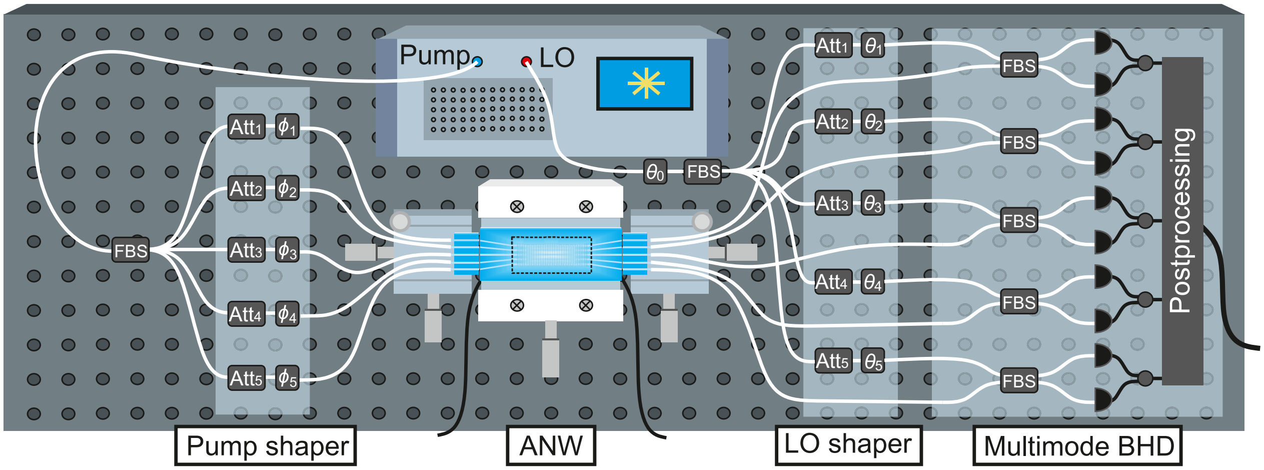

FIG. 1. Sketch of our versatile entanglement synthesizer based on an array of nonlinear waveguides (ANWs) made up of five PPLN waveguides working in a SPDC configuration (not at scale). A single laser with a second harmonic generation stage outputs coherent pump and local oscillator (LO) beams. A reconfigurable multimode shaper composed of a $1 \times N$ fiber beam splitter (FBS), attenuators (Att$_j$) and phase shifters (ϕ_j) at pump frequency inputs the desired profile ($\vec{\eta}, \vec{\phi}$) in the array through a V-groove array. Bent waveguides conduct the pump modes to the periodically poled ANWs (dashed box) where signal modes are generated and evanescently coupled. The coupling profile $\vec{f}$, wavevector phase matching and coupling phase matching can be suitably engineered for a specific operation mode. The output light is collected by V-groove arrays and directed to a multimode balanced homodyne detector (BHD). The multimode LO shaper is composed of attenuators (Att$_j$) and phase shifters (θ_j). Each independent BHD mixes the LO and SPDC light in a balanced FBS and the result is measured by a pair of photodiodes. The currents yielded by photodiodes are subtracted two by two and the generated electric signals are then electronically mixed (postprocessed) if necessary. Access to the individual mode basis is achieved simply using independent LOs. Access to the supermode bases involves shaping the LO in every single supermode through LO phase ($\vec{\theta}$) and amplitude profiles (see Secs. III B and V B).

The paper is organized as follows. In Sec. II we introduce the theoretical model for the ANWs. In Sec. III we develop and solve the propagation equations in three relevant encoding bases: individual modes, linear and nonlinear supermodes. We propose methods of detection in each basis. We then exhibit in all bases unoptimized generation of multimode squeezing using one analytical solution related to a specific pumping profile. We conclude by summarizing the main features of each encoding basis. In Sec. IV we analyze the optimized generation of multipartite entanglement in the individual mode basis. In Sec. V we focus on the versatile generation of cluster states both in terms of their geometry and encoding. Finally, in Sec. VI we discuss the different mode-basis encoding and point at applications, we present future research directions for our synthesizer, and we analyze the feasibility of our approach.

II. THE ARRAY OF NONLINEAR WAVEGUIDES

The array of nonlinear waveguides consists of N identical single-mode $\chi^{(2)}$ waveguides in which degenerate SPDC and nearest-neighbor evanescent coupling between the generated fields take place. The array can be made of, for instance, periodically poled lithium niobate (PPLN) waveguides as sketched in Fig. 1 (dashed box). In each waveguide, an input harmonic field at frequency ω_h is type-0 down-converted (same polarization modes) into a signal field at frequency ω_s [30]. We consider pump undepletion with $\alpha_{h,j}$ a strong coherent pump field propagating in the jth waveguide. We assume that the phase-matching condition $\Delta\beta \equiv \beta(\omega_h) - 2\beta(\omega_s) = 0$, with $\beta(\omega_{h,s})$ the propagation constant at frequency $\omega_{h,s}$, is fulfilled only in the coupling zone. The energy of the signal modes propagating in each waveguide is exchanged between the coupled waveguides through evanescent waves, whereas the interplay of the second harmonic waves is negligible for the considered propagation lengths due to their high confinement in the guiding region. We consider a general inhomogeneous array of N identical waveguides and continuous-wave propagating fields. The physical processes involved are described by the system of equations [28,31]

$$\frac{d\hat{\mathcal{A}}_j}{dz} = iC_0(f_{j-1}\hat{\mathcal{A}}_{j-1} + f_j\hat{\mathcal{A}}_{j+1}) + 2i\eta_j\hat{\mathcal{A}}_j^\dagger, \qquad (1)$$

where $\hat{\mathcal{A}}_0 = 0$ and $\hat{\mathcal{A}}_{N+1} = 0$, $f_0 = f_N = 0$, and $j = 1, \ldots, N$ is the individual mode index. The $\hat{\mathcal{A}}_j \equiv \hat{\mathcal{A}}_j(z, \omega_s)$ are monochromatic slowly varying amplitude annihilation operators of signal (s) photons corresponding to the jth waveguide, where $[\hat{\mathcal{A}}_j(z,\omega), \hat{\mathcal{A}}_{j'}^\dagger(z,\omega')] = \delta(\omega-\omega')\delta_{j,j'}$. The $\hat{\mathcal{A}}_j$ are thus the annihilation operators in the individual mode basis. Here $\eta_j = g\,\alpha_{h,j} \equiv |\eta_j|\,e^{i\phi_j}$ is the effective nonlinear coupling constant corresponding to the jth waveguide, with g the nonlinear constant proportional to $\chi^{(2)}$ and the spatial overlap of the signal and harmonic fields in each waveguide; $C_j = C_0 f_j$ is the linear coupling constant between modes j and $j+1$; and z is the coordinate along the direction of propagation. Both the coupling and nonlinear constants depend on the signal frequency, $C_0 \equiv C_0(\omega_s)$ and $g \equiv g(\omega_s)$. In the following, we set them as real without loss of generality.

The ANWs presents a large number of governing parameters that can be engineered to fit a desired operation and application. There are two types of parameters according to our ability to reconfigure them. (i) The evanescent coupling profile $\vec{f} = (f_1, \ldots, f_{N-1})$ [32–35], the length of the sample L, the number of waveguides N—and notably its parity—and the wavevector and coupling periodical inversion periods $(\Lambda_{\Delta\beta}, \Lambda_C)$ in quasiphase matched structures [36,37] that cannot be tuned once the sample is fabricated. In contrast, (ii) the power and phase pump profiles, respectively given by $\vec{\eta} = (|\eta_1|, \ldots, |\eta_N|)$ and $\vec{\phi} = [\arg(\eta_1), \ldots, \arg(\eta_N)]$, the coupling strength $C_0(\omega_s)$ [38], and the basis of detection [18] that can be set according to a required operation and encoding of information. The large number of degrees of freedom available in a compact device is the main advantage of the ANWs with respect to other approaches in the generation of multimode entangled states [12,13]. We demonstrate in this paper how to use these tunable parameters to generate CV multipartite entanglement and cluster states.

We first need to solve the propagation in the ANWs. Equation (1) can be solved numerically for a specific set of parameters C_j, η_j, and N, or even analytically if N is small. However, it is difficult to gain physical insight from numerical or low-dimension analytical solutions due to the increasing complexity of the system with the number of waveguides. The problem of propagation in an ANWs is simplified by using the eigenmodes of the corresponding linear array of waveguides—the linear or propagation supermodes [39]. These linear supermodes are especially useful as an intermediate step to diagonalize the evolution of the system and they are used throughout Sec. III. These supermodes are coupled through the nonlinearity. We find a further simplification by using the eigenmodes of the full nonlinear system—the nonlinear or squeezing supermodes [40]—which are squeezed and fully decoupled but local (z dependent). Thus, we use three complementary and useful bases in the ANWs: the individual mode $\mathcal{A}$, the linear supermode $\mathcal{B}$, and the nonlinear supermode $\mathcal{C}$ bases. Quantum information can be naturally encoded in any of the three bases. A suitable implementation of the detection provides access to a given encoding [41]. Below we give general solutions to the propagation problem in the three bases, discuss the methods of detection suitable for each basis (i.e. encoding), present an example with an analytical solution, and summarize the main features of the three encoding strategies.

III. GENERATION AND DETECTION OF MULTIMODE SQUEEZED STATES

A. Propagation solution in the individual mode and supermode bases

We derive below the general solutions to the propagation in the ANWs and present the different available detection methods depending on the encoding strategy. Considering coupling only between nearest-neighbor waveguides, a linear waveguide array [Eq. (1) with $\eta_j = 0$] presents supermodes $\mathcal{B}$, i.e., propagation eigenmodes. In general, any linear waveguide array is represented by a Hermitian tridiagonal matrix—Jacobi matrix—with nonnegative entries and thus by a set of nondegenerate eigenvalues and eigenvectors given in terms of orthogonal polynomials [39,42,43]. These eigenvectors (linear supermodes) form a basis and are represented by an orthogonal matrix $M \equiv M(\vec{f})$ with real elements $M_{k,j}$. The individual mode and linear supermode bases are related by $\hat{\mathcal{B}}_k = \sum_{j=1}^N M_{k,j}\,\hat{\mathcal{A}}_j$. The supermodes are orthonormal $\sum_{j=1}^N M_{k,j} M_{k',j} = \delta_{k,k'}$, and the spectrum of eigenvalues is $\lambda_k \equiv \lambda_k(C_0,\vec{f})$. We label the supermodes in a descending order with respect to their eigenvalue. We focus on the relevant case of homogeneous coupling along the propagation, i.e., C_j does not depend on z. Using slowly varying supermode amplitudes $\hat{B}_k = \hat{\mathcal{B}}_k\, e^{-i\lambda_k z}$ and the orthonormality property, the following equation for the linear propagation supermodes is obtained:

$$\frac{d\hat{B}_k}{dz} = \sum_{k'=1}^{N} \mathcal{L}_{k,k'}(z)\hat{B}^\dagger_{k'}. \tag{2}$$

The coupling matrix $\mathcal{L}(z)$ is the local joint-spatial supermode distribution of the ANWs and its elements are given by

$$\mathcal{L}_{k,k'}(z) = 2i\sum_{j=1}^{N} |\eta_j|M_{k,j}M_{k',j}\; e^{i\{\phi_j-(\lambda_k+\lambda_{k'})z\}}; \tag{3}$$

$\mathcal{L}(z)$ is a complex symmetric matrix that gathers information about the spatial shape of the pump, i.e., amplitudes and phases in each waveguide, and the propagation supermodes coupling.

Equation (2) is ubiquitous in the context of multimode squeezing [40,41]. In other approaches the coupling matrix however is constant along the propagation, i.e., $\mathcal{L}$ does not depend on z [44]. The z dependence is a unique feature of the ANWs. The general solution to Eq. (2) thus has to take into account space-ordering effects when necessary [45]. For instance, in single-pass z-dependent PDC for gains generating squeezing above 12 dB [46]. However, space-ordering effects can be neglected here since (i) a low-gain regime—small $|\eta_j|$—is crucial for individual-mode entanglement, and indeed the light generated in each waveguide remains guided without coupling if $|\eta_j| > C_0$ [47], (ii) our starting point Eq. (1) is correct for small values of C_0 since next-to-nearest-neighbor evanescent coupling should be included for large values of C_0 [39], and (iii) we study SPDC generated from a vacuum where space-ordering corrections start at the third order—roughly as $\mathcal{O}(|\eta_j|^3)$ [48]. The formal solution to Eq. (2) in this regime can thus be written as

$$\begin{pmatrix}\vec{B}(z)\\ \vec{B}^\dagger(z)\end{pmatrix} = \exp\left\{\begin{pmatrix}0 & \int_0^z \mathcal{L}(z')dz' \\ \int_0^z \mathcal{L}^*(z')dz' & 0\end{pmatrix}\right\}\begin{pmatrix}\vec{B}(0)\\ \vec{B}^\dagger(0)\end{pmatrix} \tag{4}$$

with $\vec{B} = (\hat{B}_1,\ldots,\hat{B}_N)^\top$. The solution of Eq. (4) can be simplified using the local nonlinear supermode basis $\hat{\mathcal{C}}$, given by $\hat{\mathcal{C}}_m = \sum_{k=1}^N \Upsilon^\dagger_{m,k}(z)\,\hat{B}_k$, where $\Upsilon(z)$ is a unitary matrix that diagonalizes the complex symmetric matrix $\int_0^z \mathcal{L}(z')dz'$ by a congruence transformation—the Autonne-Takagi transformation—such that $\Upsilon(z)\,[\int_0^z \mathcal{L}(z')dz']\,\Upsilon^\top(z) = \Lambda(z)$, with $\Lambda(z)$ a real diagonal matrix with non-negative entries [49]. Equation (4) in terms of nonlinear supermodes is thus simply given by

$$\hat{\mathcal{C}}_m(z) = \cosh[r_m(z)]\,\hat{\mathcal{C}}_m(0) + \sinh[r_m(z)]\,\hat{\mathcal{C}}^\dagger_m(0), \tag{5}$$

where $r_m(z) = \Lambda_{m,m}(z)$ are the down-conversion gains at a propagation distance z. Each local nonlinear supermode thus appears as a single-mode squeezed state. The z dependence of the nonlinear supermodes is a trademark of the ANWs. The evanescent coupling indeed produces a phase mismatch between the pump and the generated signal waves that results in a z-dependent interaction. This coupling-based phase mismatch affects the amount of squeezing and entanglement generated in the ANWs. The relation between the nonlinear supermodes and the individual modes is

$$\hat{\mathcal{C}}_m = \sum_{k=1}^{N}\sum_{j=1}^{N}[\Upsilon^\dagger_{m,k}(z)\,M_{k,j}\;e^{-i\lambda_k z}]\hat{\mathcal{A}}_j. \tag{6}$$

This expression encapsulates the mechanisms at play in the ANWs: the evanescent coupling generates the linear supermodes ($M_{k,j}$) that get a phase due to propagation ($\lambda_k z$) and the nonlinearity couples them locally [$\Upsilon^\dagger_{m,k}(z)$]. In terms of the individual modes, the solution to the nonlinear system is thus

$$\hat{\mathcal{A}}_j(z) = \sum_{k,m,j'=1}^{N}[M_{j,k}\Upsilon_{k,m}(z)M_{m,j'}\,e^{i\lambda_k z}] \times \{\cosh[r_m(z)]\,\hat{\mathcal{A}}_{j'}(0) + \sinh[r_m(z)]\,\hat{\mathcal{A}}^\dagger_{j'}(0)\}. \tag{7}$$

Equations (4), (5), and (7) are the general solutions to the propagation problem in the ANWs in the linear supermodes, nonlinear supermodes, and individual mode bases, respectively. These three solutions represent a resource for encoding quantum information. Our results generalize those previously obtained in driven quantum walks in ANWs [24,25,50].

Since we are interested in CV squeezing and entanglement, we also use the field quadratures $\hat{x}_j$, $\hat{y}_j$, where $\hat{x}_j = (\hat{\mathcal{A}}_j + \hat{\mathcal{A}}_j^\dagger)$ and $\hat{y}_j = i(\hat{\mathcal{A}}_j^\dagger - \hat{\mathcal{A}}_j)$ are respectively the amplitude and phase quadratures corresponding to a signal optical mode in the individual mode basis $\mathcal{A}$. Field quadratures for the linear $\mathcal{B}$ and nonlinear $\mathcal{C}$ supermodes are defined in a similar way. In the basis of individual modes, with quadratures $\hat{\xi} = (\hat{x}_1, \ldots, \hat{x}_N, \hat{y}_1, \ldots, \hat{y}_N)^\top$, the general solution of Eq. (7) can be written as $\hat{\xi}(z) = S(z)\,\hat{\xi}(0)$, with $S(z)$ a symplectic matrix that contains all the information about the propagation of the quantum state of the system. The quantum states generated in the ANWs are Gaussian. The most interesting observables in Gaussian CVs are the second-order moments of the quadrature operators, properly arranged in the covariance matrix V [51]. For a quantum state initially in a vacuum, the covariance matrix at any plane z is given by $V(z) = S(z)S^\top(z)$, with 1 the value of the shot noise related to each quadrature in our notation. Evolution of variances $V(\xi_i, \xi_i)$ and quantum correlations $V(\xi_i, \xi_j)$ can be obtained at any length from the elements of this matrix. The covariance matrix can be written as

$$V(z) = R_1(z)K^2(z)R_1^\top(z), \tag{8}$$

where we have applied a Bloch-Messiah decomposition of $S(z)$ [52], $K^2(z) \equiv K^2(\vec{\eta}, \vec{\phi}, z) = \{e^{2r_1(z)}, \ldots, e^{2r_N(z)}, e^{-2r_1(z)}, \ldots, e^{-2r_N(z)}\}$ is the covariance matrix in the nonlinear supermode basis, and $R_1(z) \equiv R_1(\vec{\eta}, \vec{\phi}, z)$ is the symplectic transformation matrix between the individual and nonlinear supermode bases, equivalent to Eq. (6) for complex fields. In fact, the Bloch-Messiah and the Autonne-Takagi approaches are fully equivalent [49]. The mth nonlinear supermode is squeezed and thus nonclassical if $K^2_{N+m}(z) = e^{-2r_m(z)} < 1$.

B. Detection schemes

The measurement of quantum noise variances and correlations is carried out by multimode balanced homodyne detection (BHD) and access to the quantum information encoded in the individual or any of the supermode bases depends on a suitable BHD realization [41]. Our photonic entanglement synthesizer is certainly compatible with a fully fibered implementation of detection via off-the-shelf telecom components, as shown in Fig. 1 [53].

The three different bases where quantum information can be naturally encoded in the ANWs correspond to different choices and engineering of LOs in multimode BHD. (i) In the individual mode basis each LO is independent. Only two detectors are necessary in order to completely characterize any multimode quantum state. The variance measured in each mode and the quantum correlations between any pair of modes allow us to reconstruct the full covariance matrix associated with the generated quantum state. Beyond quantum state tomography, to perform a quantum information protocol, it is necessary to use the same number of LOs and detectors in the multimode BHD as the number of modes involved in the protocol. (ii) The detection in an arbitrary supermode basis is based on the combination of the SPDC output fields with a spatially reconfigurable multimode local oscillator (LO shaper in Fig. 1), a spatial analogue to what has been pioneered in the spectral domain in Ref. [18]. The LO shaper sets the relative amplitudes and phases of the multimode LO to select a given supermode, and a controllable global phase (θ_0 in Fig. 1) selects the quadrature to be measured [54,55]. This shaped LO can indeed be set successively as the elements of a supermode basis enabling the measurement of the full covariance matrix in that basis. This measurement method can be implemented in fibered or in bulk optics respectively through fibered multimode BHD or bulk-optics single-mode BHD with a spatially shaped LO. We note that every pump configuration and length of the sample L produces a different nonlinear supermode basis as stated by Eq. (6). Thus, the detection basis has to be reconfigured for every pump distribution when this encoding strategy is selected. Our theoretical model is hence crucial for determining the operation and fabrication parameters of the ANWs so that it provides a sought-after operation.

C. Example: squeezing in the three mode bases for a flat pump profile

Suitable manipulation of individual power and phase pump fields by means of off-the-shelf elements as fiber attenuators and phase shifters, and V-groove arrays linking the fiber-optics elements to the ANWs enable an on-demand pump distribution engineering (Fig. 1). The pump profile couples the propagation supermodes generating the joint-spatial supermode distribution given by Eq. (3). In general, this generates complicated connections between the linear supermodes. However, the orthogonality and symmetry properties of the linear supermodes lead to analytical solutions in some cases. An outstanding simplification of the system is obtained when pumping all the waveguides with the same power and phase, which we refer to as the flat pump profile. We now discuss the features of this configuration in the three bases.

Linear supermode basis. When all waveguides are equally pumped such that $\eta_j = \eta$, Eq. (3) is notably simplified to $\mathcal{L}_{k,k'}(z) = 2i\eta\delta_{k,k'}\exp[-i(\lambda_k + \lambda_{k'})z]$, where we have used the orthonormality of the linear supermodes. This pump configuration diagonalizes the joint-spatial distribution, making every linear supermode independently squeezed. The solution of Eq. (2) in terms of linear supermodes $\mathcal{B}_k$ can then be written as

$$\hat{\mathcal{B}}_k(z) = \cos(F_k z)\hat{\mathcal{B}}_k(0) + i\frac{\sin(F_k z)}{F_k}[\lambda_k \hat{\mathcal{B}}_k(0) + 2\eta\, \hat{\mathcal{B}}_k^{\dagger}(0)] \tag{9}$$

with $F_k = \sqrt{\lambda_k^2 - 4|\eta|^2}$. This solution is exact for any gain regime [45]. It generalizes the solution found for the nonlinear directional coupler ($N = 2$) in Ref. [56] and remains valid for any number of waveguides N, evanescent coupling profile $\vec{f}$, and propagation distance z. Note that, for $|\lambda_k| > 2|\eta|$ and $|\lambda_k| < 2|\eta|$, Eq. (9) is respectively the solution of a nonphase-matched and phase-matched degenerate parametric amplifier [57]. For typical evanescent coupling, nonlinearities, and pump powers found in a quadratic ANWs, F_k is real for the majority of supermodes. In this case, the kth propagation supermode periodically oscillates between a maximum and zero with oscillation periods $L_k = \pi/(2F_k)$. The period L_k depends on the pump power and, markedly, on the evanescent coupling profile $\vec{f}$ through λ_k. Interestingly, waveguide arrays with an odd number of identical waveguides N exhibit a propagation eigenmode with zero eigenvalue $\lambda_{(N+1)/2} = 0$ [42]. This supermode is phase matched all along the propagation and its squeezing is maximum [58].

We exhibit the features discussed above with a specific example in an array with $N = 5$ waveguides. In Fig. 2(a) we show the evolution of maximum linear supermode squeezing $\{V[y_k(\theta_k), y(\theta_k)] < 1\}$ over a generalized phase quadrature $y_k(\theta_k)$ [59]. We set the kth LO phase as $\theta_k(z)$, maximizing the kth linear supermode squeezing [45]. We set $|\eta| = 0.015$ mm^{-1}, a realistic value comparable with that obtained in Ref. [23]. We choose a homogeneous coupling profile $f_j = 1$. The propagation constants related to each propagation supermode with this coupling profile are $\lambda_k = 2C_0 \cos[k\pi/(N+1)]$ [39]. We show the effect of the coupling strength C_0 on the squeezing with three different cases: 0.08 mm^{-1} (dashed), 0.24 mm^{-1} (solid), and 0.72 mm^{-1} (dotted). The $k = 3$ supermode is the only nondegenerate supermode (green). It is independent of the value of C_0, builds up continuously, and is efficiently squeezed. The amount of squeezing is degenerate two by two for the other supermodes. The maximum squeezing in these supermodes ($k = 1, 5$ in blue, $k = 2, 4$ in orange) decreases as the coupling strength C_0 increases.

The properties of the linear supermodes thus give insight into the properties of the squeezed light generated in the array in this pump configuration. We have found and analyzed similar analytical solutions for other pump configurations in this basis [45].

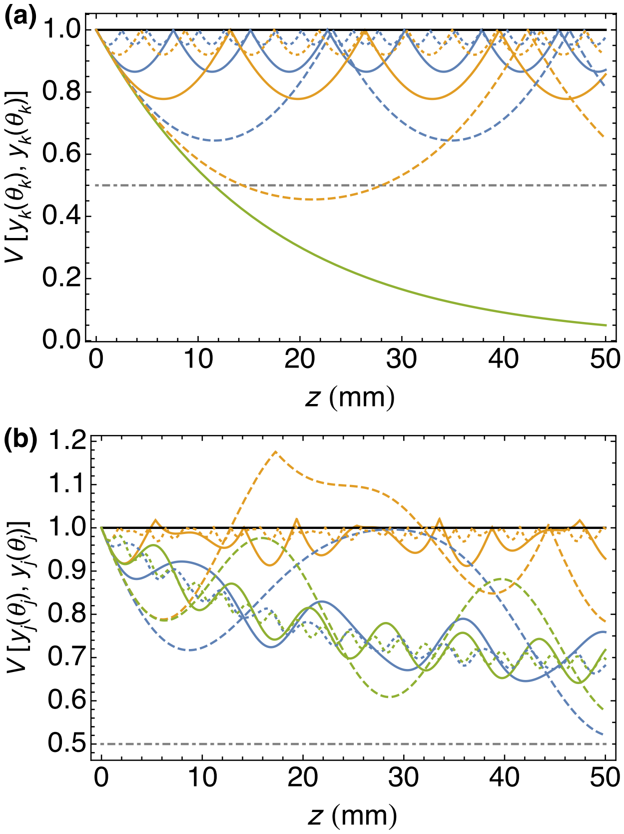

FIG. 2. Evolution of squeezing in a five-waveguides homogeneous coupling profile nonlinear array pumping with a flat pump profile. (a) Maximum linear supermode squeezing $\{V[y_k(\theta_k), y(\theta_k)] < 1\}$. Equivalent curves are retrieved for nonlinear supermode squeezing. The $k = 3$ supermode is efficiently squeezed independently of the coupling strength (green). The other supermodes are degenerate two by two: $k = 1, 5$ (blue) and $k = 2, 4$ (orange). (b) Maximum individual mode squeezing $\{V[y_j(\theta_j), y_j(\theta_j)] < 1\}$ for $j = 1, 5$ (blue), $j = 2, 4$ (orange) and $j = 3$ (green). The dashed, solid, and dotted lines respectively denote $C_0 = 0.08, 0.24$, and 0.72 mm^{-1}. Here $\eta = 0.015$ mm^{-1}. The gray dash–dot line denotes the 3 dB squeezing level.

Nonlinear supermode basis. The flat pump configuration diagonalizes directly the system in the linear supermode basis. After an appropriate phase-space rotation, carried out by the LO in the multimode BHD, the system is fully diagonal in the phase space and thus linear and nonlinear supermodes are degenerate. Note that, for the example presented above, the nonlinear supermodes obtained via Autonne-Takagi (or Bloch-Messiah) diagonalization exhibit the same levels of squeezing $K^2_{N+m}(z)$ (not shown) as those shown in Fig. 2(a) for linear supermodes, but a different spatial profile at each propagation length z [45].

Individual mode basis. The solution in the individual mode basis is straightforwardly obtained from Eq. (9) with the basis change $\hat{\mathcal{A}}_j = \sum_{k=1}^{N} M_{k,j}\, \hat{\mathcal{B}}_k$. Note that this is analogous to inputting a set of N independently squeezed states in an $N \times N$ interferometer given by the orthogonal matrix $M \equiv M(\vec{f})$. This configuration can thus produce entanglement in the individual mode basis, as we show in the next section.

In Fig. 2(b) we show the evolution of maximum individual mode $\mathcal{A}_j$ squeezing $\{V[y_j(\theta_j), y_j(\theta_j)] < 1\}$ over a generalized phase quadrature $y_j(\theta_j)$ [59] for the same configuration and coupling strengths as in Fig. 2(a). In this case we independently set the LO phase of each BHD as $\theta_j(z)$ to maximize the squeezing of the jth individual mode. Note that there are distances where the individual mode squeezing for modes $j = 2, 4$ (orange) is over the shot noise. In contrast to the linear supermode case, the evolution of squeezing is complex in the individual mode basis and it is difficult to obtain physical insight directly from it. Moreover, this configuration presents quantum correlations (not shown) that can lead to entanglement.

The possibilities of our concept go nonetheless considerably beyond the flat pump profile. The ANWs presents a large number of degrees of freedom that can be suitably tuned in order to yield a desired mode of operation. We tackle this question in depth and exhibit the versatility of the ANWs, addressing a crucial and fundamental issue in quantum information processing, the generation of multipartite entanglement. We showcase two remarkable axes in the most appropriate encoding: in Sec. IV, partial numerical optimization on the pump phase profile in the individual mode basis, and in Sec. V, full numerical optimization on all available parameters to demonstrate versatility in the individual mode basis and in optimized nonlocal bases built from nonlinear supermodes.

D. Encoding strategies summary

To end this section, we sketch an informal practical landscape of the introduced bases in the ANWs. (i) The elements of the individual mode basis $\mathcal{A}$ are modes associated with a single waveguide, and they can be distributed to spatially distant locations. All elements of this basis can be jointly measured and the detection basis is fixed. Squeezing is not optimal in this basis. It is directly connected to applications in quantum networks and can be used in existing communication, sensing, and computing protocols (see Sec. VI and especially Table II). (ii) The elements of the linear supermode basis $\mathcal{B}$ are collective modes. Only one mode can be measured at a time and the detection basis is fixed (pump profile and device length independent). Squeezing is in general not optimal. Basis $\mathcal{B}$ is useful to derive trends analytically [45], as in Fig. 2(a), which can be applied to the other encodings ($\mathcal{A}$, $\mathcal{C}$) and this basis is well suited to quantum simulation. (iii) The elements of the nonlinear supermode basis $\mathcal{C}$ are collective modes. Only one mode can be measured at a time and the detection basis is variable (pump profile and device length dependent). Squeezing is optimal in this basis. Entanglement is engineered in the measurement stage. It is close to a rich niche in the spectral domain [16–18] and is well suited to engineer quantum states and study their features.

IV. MULTIPARTITE ENTANGLEMENT OF INDIVIDUAL MODES IN THE ANWs

Multipartite entangled states are a key resource for quantum computing, through the measurement-based framework [5,6], and for quantum key distribution networks, obtaining higher secret key rates with respect to bipartite entangled states and extending the range of application through all-photonic quantum repeaters [60,61]. Measuring multipartite full inseparability in CV systems requires the simultaneous fulfillment of a set of conditions that leads to genuine multipartite entanglement when pure states are involved [62]. These inequalities, known as the van Loock-Furusawa (VLF) criterion, can be easily calculated from the elements of the covariance matrix V in a given basis. Full N-partite inseparability is guaranteed if the following $N - 1$ inequalities are simultaneously violated in a basis with modes labelled by i [62]:

$$\begin{aligned}\rho_i &\equiv V[x_i(\theta_i) - x_{i+1}(\theta_{i+1})] \\ &\quad + V\left[y_i(\theta_i) + y_{i+1}(\theta_{i+1}) + \sum_{i' \neq i,i+1}^{N} G_{i'}\, y_{i'}(\theta_{i'})\right] \\ &\geq 4. \end{aligned} \tag{10}$$

Here $x_i(\theta_i)$ and $y_i(\theta_i)$ are generalized quadratures [59], $\vec{\theta} \equiv (\theta_1, \ldots, \theta_N)$ is the measurement LO phase profile, $\vec{G} \equiv (G_1, \ldots, G_N)$ are N real parameters that are set by optimization—a BHD gain profile [63].

In general, we can prepare the state in such a way that the generated SPDC light is multipartite entangled. In other words, we find that there is a set of pump amplitude $\vec{\eta}$ and phase $\vec{\phi}$ profiles, as well as LO phase $\vec{\theta}$ and BHD gain $\vec{G}$ profiles, which minimize the value of Eq. (10) for a given set of fixed parameters of the array—coupling profile $\vec{f}$, number of waveguides N, and length of the sample L—and choice of encoding. Below we demonstrate that the ANWs is a versatile source of multipartite entanglement through optimization. We choose the individual mode basis as the measurement basis as it is the most accessible basis and entanglement can be distributed in a network, and compare the entanglement among these modes produced by the flat pump profile introduced in Sec. IV, where only the BHD parameters $\{\vec{G}, \vec{\theta}\}$ can be tuned, with the entanglement yielded if the pump phase profile is also tuned $\{\vec{\phi}, \vec{G}, \vec{\theta}\}$ in an optimization procedure. Note that the elements of the linear supermode basis can also be entangled. By contrast, the elements of the nonlinear supermode basis are not entangled, i.e., independent, but they can be used as

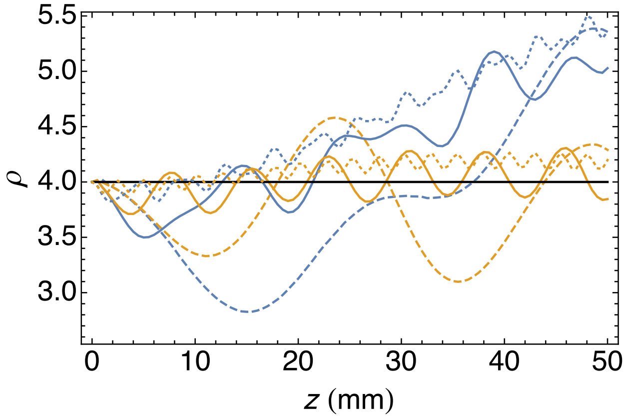

FIG. 3. Multipartite entanglement in the individual mode basis versus propagation for a flat pump profile ($|\eta_j| = |\eta|$, $\Delta\phi = 0$) in a five-waveguides ANWs. BHD parameters $\{\vec{G}, \vec{\theta}\}$ are set in order to optimize the violation of the van Loock-Furusawa inequalities ρ_j. Simultaneous values under the threshold value $\rho = 4$ (black) imply CV pentapartite entanglement (four inequalities, degenerate two by two; blue and orange curves). The dashed, solid, and dotted lines denote $C_0 = 0.08, 0.24$, and 0.72 mm^{-1}, respectively. Here $\eta = 0.015$ mm^{-1}.

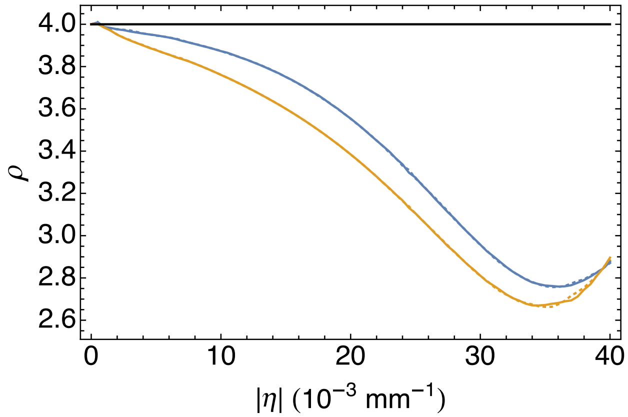

FIG. 4. Multipartite entanglement in the individual mode basis versus flat pump-power profile ($|\eta_j| = |\eta|$, $\Delta\phi \neq 0$) in a five-waveguides ANWs. BHD parameters $\{\vec{\phi}, \vec{G}, \vec{\theta}\}$ are set in order to optimize the violation of the van Loock-Furusawa inequalities ρ_j. Simultaneous values under the threshold value $\rho = 4$ (black) imply CV pentapartite entanglement (four inequalities, $N = 5$). We let $j = 1$ (dotted blue), $j = 2$ (dotted orange), $j = 3$ (solid orange), $j = 4$ (solid blue), $C_0 = 0.24$ mm^{-1}, and $z = 30$ mm.

a starting point to engineer entangled states through suitable transformations. More details are presented in Secs. V and VI.

Firstly, as an example of a nonoptimal procedure, we focus on the cases shown in Fig. 3: an $N = 5$ ANWs with a homogeneous coupling profile $f_j = 1$ and a flat pump-power distribution ($|\eta_j| = |\eta|$, $\Delta\phi = \phi_{j+1} - \phi_j = 0$). We analyze the impact of the coupling strength C_0 on the multipartite entanglement; as noted in Figs. 2(a) and 2(b), it has an impact on squeezing. In this case we set the individual mode basis and adapt the detection, i.e., the BHD parameters: the LO phases $\vec{\theta}$ and the electronic gains $\vec{G}$. We use the sum of the four inequalities $F_M(\vec{G}, \vec{\theta}) = \sum_{j=1}^{4} \rho_j$ as the fitness function to optimize. We use an evolution-strategy algorithm to tackle optimization problems [64]. Our optimization algorithm adjusts ten parameters to find the minimum of F_M. In Fig. 3 we show two-by-two degenerate inequalities found for three different values of the coupling strength C_0: 0.08 mm^{-1} (dashed), 0.24 mm^{-1} (solid), and 0.72 mm^{-1} (dotted). The three cases present regions where fully multipartite entanglement is achieved ($\rho_j < 4$). The lower the value of C_0, the larger the violation of the inequalities, as expected from Fig. 2(a).

Let us move now to a further optimized example. We study the same ANWs at a fixed length $z = 30$ mm and coupling strength $C_0 = 0.24$ mm^{-1} where we can additionally tune the individual pump phases ($|\eta_j| = |\eta|$, $\Delta\phi \neq 0$). Note that there is no entanglement at this distance for $\Delta\phi = 0$, as shown in Fig. 3 ($\rho_{1,4} = 4.51$ solid blue, $\rho_{2,3} = 4.23$ solid orange). We again use the sum of the four inequalities $F_M(\vec{\phi}, \vec{G}, \vec{\theta})$ as the fitness function to optimize, now with four extra parameters related to the relative pump phases. In Fig. 4 we show the four inequalities for five propagating modes for different values of the power per waveguide $|\eta|$, among them $|\eta| = 0.015$ mm^{-1}, the case shown in Fig. 3. Genuine multipartite entanglement is obtained for each value of $|\eta|$ shown. Remarkably, the simultaneous violation of the four inequalities at $|\eta| = 0.015$ mm^{-1} by only optimizing the pump phases exhibits the versatility of our approach. Note that the above optimization procedure represents a lower bound on the violations based on the fitness function we have chosen and our optimization algorithm. Hence, there can be other sets of parameters that present larger violations of the VLF inequalities.

In the next section we broaden the spectrum of applications of the ANWs to the optimized generation of multipartite states with a specific geometry: the cluster states. The interest in these states lies in that they are the essential resource of MBQC and one of the main actors in the quest for a photonic quantum computer [65].

V. OPTIMIZATION OF CLUSTER STATES

MBQC relies on the availability of a large multimode entangled state on which a specific sequence of measurements is performed. The choice of natural or exotic bases widens the range of application in MBQC [66]. In our case the cluster states can be encoded in the individual mode basis or any other basis of the array.

An ideal CV cluster state is a simultaneous eigenstate of specific quadrature combinations called nullifiers [5,6].

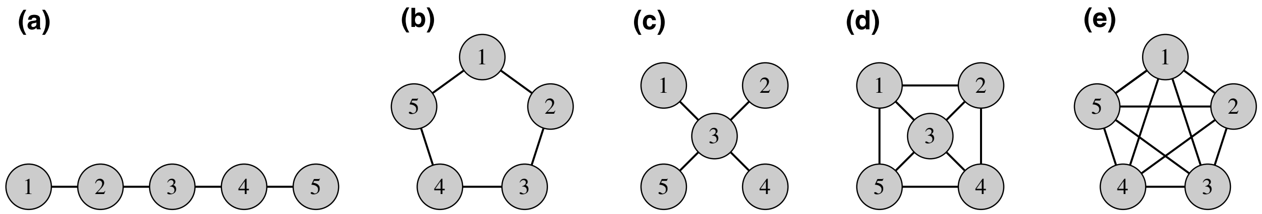

FIG. 5. Some five-node graphs generated in the ANWs. (a) Linear, (b) pentagon, (c) star, (d) square pyramid, and (e) maximally connected pentagon [also known as the Greenberger-Horne-Zeilinger (GHZ) graph].

Cluster states are associated with a graph or adjacency matrix J reflecting those nullifiers. The nodes of the graph represent the modes of the cluster state in a given basis, and the edges the entanglement connections among the modes. Moreover, the labeling of the nodes can be suitably set to maximize the entanglement. The nullifiers are given by

$$\hat{\delta}_i \equiv \hat{x}_i\left(\theta_i + \frac{\pi}{2}\right) - \sum_{i'=1}^{N} J_{i,i'}\,\hat{x}_{i'}(\theta_{i'}) \quad \text{for all } i = 1, \ldots, N, \tag{11}$$

where J is the adjacency matrix and $\hat{x}_i(\theta_i)$ is the ith generalized quadrature in a given basis [59]. We consider unit-weight cluster states with $J_{i,i'} = 1$ for modes i and i' being nearest neighbors in the graph and all the other entries of J are zero. The variances of the nullifiers tend to zero in the limit of infinite squeezing. Experimentally, a cluster state can be certified if two conditions are satisfied: (i) the noise of a set of normalized nullifiers lies below the shot noise threshold, i.e.

$$V(\bar{\delta}_i) < 1 \quad \text{for all } i = 1, \ldots, N, \tag{12}$$

where $\bar{\delta}_i \equiv \delta_i/\sqrt{1+n(i)}$ is the normalized nullifier and $n(i)$ is the number of nearest neighbors to the ith node of the cluster, and (ii) the cluster state is fully inseparable, i.e., it violates a set of VLF inequalities [11,62].

As the encoding of quantum information is mode-basis dependent, building on the formalism and measurement possibilities of Sec. III we demonstrate the versatility of our platform by presenting two strategies for cluster-state generation: one where the individual modes are set as the nodes of the cluster, and another based on nonlinear supermodes. We exhibit below how optimized configurations can produce the different types of clusters shown in Fig. 5, focusing on the individual mode basis, and discuss applications of both encoding schemes in Sec. VI.

A. Individual modes as nodes of the cluster

In the individual mode basis, we set the simplest labeling: the ith node of the graph corresponds to the jth mode. The large size of the parameter space corresponding to the ANWs enables the optimized generation of different classes of cluster states. We use the sum of the five nullifier variances $F_C(\vec{\eta}, \vec{\phi}, \vec{\theta}) = \sum_{i=1}^{5} V(\bar{\delta}_i)$ with 15 free parameters as the fitness function to minimize. For the sake of comparison, we use the same parameters as in the previous section, i.e., a homogeneous coupling profile $f_j = 1$ with coupling strength $C_0 = 0.24\ \text{mm}^{-1}$ and a fixed length $z = 30$ mm. In Table I we detail the optimized nullifier variances obtained for the $N = 5$ node cluster states shown in Fig. 5. Remarkably, we find realistic sets of parameters $\{\vec{\eta}, \vec{\phi}, \vec{\theta}\}$ to generate the clusters in the five analyzed cases. In particular, the linear cluster is optimized with a pump profile very close to the flat one that we introduced in Sec. III. We use here the same set of pump parameters for optimizing star-shaped and GHZ clusters, since both are related by only local oscillator phase shifts [67]. Full inseparability of the generated states is ensured using the variances of the nullifiers exhibited in Table I in the expressions shown in Appendix A. We have checked this approach on cluster-state generation with up to $N = 15$ modes, obtaining similar values of nullifier variances for realistic parameters (not shown). Note that the use of a different fitness function or node labeling can lead to different values of nullifier variances. Therefore, the generation of cluster states in a fixed detection basis is possible in the ANWs. Enough degrees of freedom in the pump and the detection are available to compensate for the monolithic coupling structure of the array and yield significant entanglement.

B. Cluster states based on nonlinear supermodes

Lower nullifier variances and hence closer-to-ideal cluster states can be obtained using a nonfixed custom detection basis. As introduced in Sec. III, the covariance matrix measured at the output of the ANWs can indeed be diagonalized by a Bloch-Messiah decomposition through Eq. (8), leading to nonlinear supermodes. Likewise, the covariance matrix associated with a given N-mode cluster V_C can be constructed from N-phase squeezed input states. We write $V_C = S_C \bar{K}^2(\vec{r}) S_C^{\top}$, where S_C is the symplectic and orthogonal transformation—a change of mode basis—which produces the cluster associated with J, and $\bar{K}^2(\vec{r})$ is a symplectic diagonal matrix that stands for phase-squeezed states. The elements of $\vec{r}$ are the squeezing

TABLE I. Individual mode basis cluster-state generation in a five-waveguides ANWs with homogeneous coupling profile for the linear, pentagon, star, square pyramid, and GHZ graphs. We show the value of the nullifiers $\{V(\bar{\delta}_i)\}$, pump-power profile $\vec{\eta}$, pump phase profile $\vec{\phi}$, and local oscillator phase profile $\vec{\theta}$. Simultaneous values of $V(\bar{\delta}_i)$ under the shot noise threshold $V(\bar{\delta}_i) = 1$ are a signature of successful cluster generation. Here $C_0 = 0.24\ \mathrm{mm}^{-1}$ and $z = 30$ mm.

Graph	Nullifiers $[V(\bar{\delta}_i)]$	$\vec{\eta} \times 10^2\ \mathrm{mm}^{-1}$	$\vec{\phi}/\pi$	$\vec{\theta}/\pi$
Linear	$\{0.20, 0.39, 0.37, 0.38, 0.20\}$	$\{9.2, 8.9, 9.1, 9.1, 9.2\}$	$-0.50 \times \{1, 1, 1, 1, 1\}$	$\{0, 0, 0, 0, 0\}$
Pentagon	$\{0.59, 0.73, 0.09, 0.34, 0.11\}$	$\{8.7, 4.9, 3.4, 1.9, 8.7\}$	$\{1.59, 0.87, 1.06, 1.34, 0.63\}$	$\{0.60, 0.19, -1.00, -0.88, 0.20\}$
Star	$\{0.40, 0.41, 0.54, 0.41, 0.40\}$	$\{6.1, 3.4, 9.5, 3.4, 6.1\}$	$\{1.02, 0.02, 0.02, 0.01, -0.98\}$	$\{-0.24, 0.26, 0.26, 0.26, -0.24\}$
Pyramid	$\{0.33, 0.12, 0.57, 0.18, 0.19\}$	$\{4.3, 9.3, 0.0, 7.3, 3.0\}$	$\{-0.11, 0.22, 0.65, 1.29, 1.00\}$	$\{0.05, 0.27, 0.40, -0.80, 0.00\}$
GHZ	$\{0.40, 0.41, 0.54, 0.41, 0.40\}$	$\{6.1, 3.4, 9.5, 3.4, 6.1\}$	$\{1.02, 0.02, 0.02, 0.01, -0.98\}$	$\{0.26, 0.76, 0.26, 0.76, 0.26\}$

parameters corresponding to each mode of encoding. Thus, setting the nonlinear supermodes as the basis, the cluster is built from, i.e., $K^2(\vec{\eta}, \vec{\phi}, z) = \bar{K}^2(\vec{r})$, the cluster and the ANWs covariance matrices are related by

$$V_C = S_{\mathrm{LO}}(\vec{\eta}, \vec{\phi}, \vec{\varphi}, z) V(z) S_{\mathrm{LO}}^{\top}(\vec{\eta}, \vec{\phi}, \vec{\varphi}, z), \tag{13}$$

where $S_{\mathrm{LO}}(\vec{\eta}, \vec{\phi}, \vec{\varphi}, z) = S_C \bar{O}(\vec{\varphi}) R_1^{\top}(\vec{\eta}, \vec{\phi}, z)$ is a symplectic and orthogonal matrix and $\bar{O}(\vec{\varphi})$ is an orthogonal matrix related to the freedom of distributing the degree of squeezing among the cluster nodes (see Appendix B). Then, the covariance matrix associated with the cluster state can be retrieved from that related to the ANWs via S_{LO}. Below we show two different ways to access cluster states with this encoding.

The first approach is to use a LO with a spatial profile given by the complex representation of S_{LO}. As discussed in Sec. III B, this can be carried out by means of a single-mode free-space BHD or via a multimode fibered BHD analogously to what was done in the spectral domain [18]. In the present case any cluster is reachable through suitable shaping of a multimode LO with common phase and amplitude references (see Fig. 1). Thus, what is to optimize is the distribution of squeezing among the different nonlinear supermodes, i.e., the elements of $K^2(\vec{\eta}, \vec{\phi}, z)$ [44]. Once the squeezing is optimized, the multimode LO is shaped using the profile of $S_{\mathrm{LO}}(\vec{\eta}, \vec{\phi}, \vec{\varphi}, z)$ to measure each nullifier.

The second approach is based on the emulation of the statistics of a given cluster state. This is carried out with a multimode fibered BHD with independent single-mode LOs and postprocessing the photocurrents coming from every detector [16,66]. In this case the transformation S_{LO} can be decomposed as $S_{\mathrm{LO}} = \bar{O}_{\mathrm{post}}(\vec{\vartheta}) D_{\mathrm{LO}}(\vec{\theta})$, where $D_{\mathrm{LO}}(\vec{\theta})$ and $\bar{O}_{\mathrm{post}}(\vec{\vartheta})$ are transformations associated with the LO phase profile and the postprocessing gains, respectively (see Appendix B). Note that emulation and LO shaping are not conceptually different, but related to the BHD detection scheme experimentally available. We show a detailed example of this approach with the cluster states of Fig. 5 in Appendix B.

The nullifiers associated with any N-dimensional cluster state can thus be directly measured with a suitably shaped LO via Eq. (13), or approximately emulated by postprocessing. Moreover, a large class of Gaussian computations can be performed replacing S_C by $S_C^{'} = U_{\mathrm{comp}} S_C$, with U_{comp} the orthogonal matrix associated with the required computation [66,68].

VI. DISCUSSION AND PERSPECTIVES

We first finish discussing the encoding and processing of information in different mode bases. We then give perspective on the range of applications of ANW-based quantum information processing, and we finally discuss the feasibility of our approach.

The individual mode basis is a natural basis to implement cluster states in the spatial domain due to a simple detection scheme [11]. This basis is however harder to implement in other domains, for instance in the spectral domain [44]. As we have demonstrated above, the ANWs is a versatile source of cluster states with this straightforward encoding. The nonlinear supermode basis offers an even higher flexibility through postprocessing or shaping the basis of detection at the cost of an increased complexity in the detection setup.

Let us compare both the encoding schemes of quantum information we have introduced above, the individual mode basis, and the nonlinear supermode basis in terms of their respective abilities in quantum information processing and quantum networks—or quantum graphs [69]. In the individual mode basis the measurement basis is fixed. The quantum network is physically yielded by the array with spatially distant nodes, which allows simultaneous access to all the nodes of the network and the detection is addressed by independent BHDs. See Table II for a summary of possible applications of the cluster states shown in Fig. 5 or similar. In contrast, any other basis based on nonlinear supermodes does not have a fixed measurement basis as the supermodes change at every propagation distance. The quantum graph is produced by LO shaping or emulated by postprocessing. Each node is encoded in the whole profile of the output SPDC light, allowing access to only one node of the network at a time. The resource of both quantum networks and graphs is entanglement. However, multimode entanglement relies on both

TABLE II. Some applications of individual mode-based cluster states generated in an ANWs.

Graph	Application	Reference(s)
Linear	Single-mode quantum computing	[70]
Square (plus time multiplexing)	Universal quantum computing	[7,8]
Star and GHZ	Anonymous broadcasting	[71,72]
Pyramid	Quantum secret sharing	[20]
Any of the above	Distributed quantum sensing	[21]

the quantum state and measurement process [18]. Thus, even single-mode squeezed states in the individual mode basis encoding can produce quantum graphs in the nonlinear supermode-based encoding with a suitable detection. This basis has been used, for instance, to simulate a quantum secret sharing protocol [18].

We now assess the usefulness of both approaches in terms of a specific quantum protocol like MBQC. The individual mode basis enables sequential or one-shot MBQC. Remarkably, universal single-mode Gaussian operations are possible using linear cluster states, homodyne detection, and classical postprocessing [12,70]. It is particularly easy in this basis to couple the state to be computed to the cluster by means of a 3 dB fibered beam splitter. Thus, the individual mode basis is a convenient basis for traditional MBQC. Direct Gaussian MBQC is possible in the nonlinear-supermode postprocessing approach; however, it is not universal in general [68]. Two-dimension cluster states are required for the most general universal MBQC [6]. Recently, the generation of this class of states has been demonstrated using spatial- and time-domain multiplexing [7,8]. The level of squeezing necessary to implement fault-tolerant MBQC is nevertheless far from technologically available [73]. Fault-tolerant MBQC is potentially realizable with lower squeezing thresholds by using cluster states of higher dimension [74]. It is then foreseeable that future MBQC will be based on multiplexing the CV modes in space, time, frequency, or angular momentum, and on integration on chip [75]. The ANWs represents a potential platform to implement that technology as the spatial encoding can be multiplexed in frequency and time in the pulsed regime.

We now discuss possible research directions that follow from this work. The first is emulation of quantum complex networks [14]. The dynamics of an ensemble of quantum harmonic oscillators linked according to a specific topology can be mapped to our multimode platform through the symplectic propagator $S(z)$ of Sec. III. The temporal evolution of a quantum network $S_{\mathrm{net}}(t)$ is directly mapped to our propagator $S(z)$, which can be experimentally realized by adequate pump profile optimization and multimode BHD. The tunability of our approach enables the study of different network topologies with a single setup.

Another interesting feature of an integrated ANWs is the possibility to include non-Gaussian operations on the quantum state, the cornerstone of quantum advantage in CV MBQC. Single-photon subtraction can indeed be implemented by means of introducing defects in the array, i.e., a weakly coupled single waveguide in between two arrays of nonlinear waveguides in such a way that the detection of a single photon de-Gaussifies and entangles the propagating quantum states related to each array [76,77].

Additionally, besides the practical applications in CVs previously discussed such as quantum secret sharing and MBQC, an appealing exploitation of the ANWs in DVs is Gaussian boson sampling (GBS) [78]. As every N-mode Gaussian state generated in the array can be decomposed by Autonne-Takagi (Bloch-Messiah) into N single-mode squeezers in between two linear interferometers, the sampled photon pattern at the output of the ANWs enables the computation of the hafnian of the matrix that characterizes the quantum state. Moreover, the ANWs operating in the SPDC or optical parametric amplification regimes can be a suitable platform for the simulation of molecular vibronic spectra through GBS [79–81].

Finally, we discuss the feasibility of our approach with respect to the state of the art in integrated CVs. The pump coherence along its profile and with the local oscillator is crucial to the generation and appropriate detection of the generated states. Mechanical and thermal stabilities similar to those currently achieved in single PPLN waveguides are expected to be achieved in the experimental implementation of our multiport scheme [23]. Both pump and detection schemes are suitable to be integrated on chip, limiting issues associated with pump phase noise [82,83]. Waveguides a few microns wide and waveguide spacing of the order of tens of microns are within the scope of standard technology [30]. The required homogeneity in nonlinearity and coupling is well within what is routinely achieved by current technology and one of the strengths of our proposal is that many external parameters (pump and LO profile, postprocessing) can compensate for imperfections. Current 127-μm-spacing commercial V-groove arrays limit the maximum number of waveguides of the ANWs. The larger the number of waveguides, the longer the chip in order to avoid the losses related to the bends in the input-output waveguiding region. With proton-exchange technology we estimate $N \approx 8$–16 waveguides as reasonable [30,83]. The limiting factor of the integration density can be overcome with nanophotonic nonlinear technologies [84,85]. The influence of losses on the CV entanglement can be included in our analysis by standard methods [37]. Propagation losses have a small impact on squeezing and entanglement, assuming typical values in PPLN waveguides (approximately equal to 0.14 dB cm^{-1}) and sample lengths (2–3 cm) [23,83]. Nonlinearities as high as $g = 24 \times 10^{-4}$ mm^{-1} mW$^{-1/2}$, and coupled cw pump powers ranging from tens to hundreds of milliwats, have recently been shown in soft proton exchange and ridge PPLN waveguides [83,86]. A squeezing level as high as −6.3 dB with cw pumping has recently been demonstrated in a PPLN chip [86]. Furthermore, nanophotonic PPLN waveguides promise to increase the nonlinear efficiency by one order of magnitude [84,85]. The pump profile engineering can be realized by means of telecom off-the-shelf elements such as fiber attenuators, phase shifters, and *V*-groove arrays, or by means of active elements in electro-optics materials such as LN [23]. An overall squeezing detection efficiency of 94% has recently been reported using antireflection coating on the chip output facet and balanced-homodyne-detector photodiodes with 99% quantum efficiency [86]. The use of *V*-groove arrays to fiber the output light can also lead to balanced-homodyne-detector spatial mode-matching visibilities of 99%.

In conclusion, we have demonstrated that the array of nonlinear waveguides is a versatile synthesizer of spatial multimode squeezing and multipartite entanglement. The tuning knobs available in the array of nonlinear waveguides enable a formidable degree of reconfigurability in a compact device. We have in particular introduced a general formalism to analyze the generation of quantum states in nonlinear waveguide arrays. We have shown versatile and significant multipartite entanglement in the experimentally most convenient basis—the individual mode basis. We have theoretically demonstrated that various cluster states appropriate for quantum networks and measurement-based quantum computing can be generated in arrays of nonlinear waveguides with the same optical setup, using pump and measurement shaping. Features such as scalability, reconfigurability, subwavelength stability, reproducibility, and low cost make this platform an appealing quantum technology in the spatial encoding domain with respect to previous bulk-optics-based multipartite-entanglement approaches. The analysis carried out here demonstrates that the array of nonlinear waveguides is a competitive contender for quantum communication, quantum computing, and quantum simulation.

ACKNOWLEDGMENTS

The authors thank G. Patera for insightful comments. This work is supported by the Agence Nationale de la Recherche through the INQCA project (Grants No. PN-II-ID-JRP-RO-FR-2014-0013 and No. ANR-14-CE26-0038), the Paris Ile-de-France region in the framework of DIM SIRTEQ through the project ENCORE, and the Investissements d'Avenir program (Labex NanoSaclay, reference ANR-10-LABX-0035).

APPENDIX A

Below we define the five normalized nullifiers and four VLF inequalities corresponding to the five-node cluster states exhibited in Fig. 5. Table I encodes node *i* in the individual mode *j* $(i = j = 1, \ldots, 5)$. Table III of Appendix B encodes node *i* in the nonlinear supermode *m* $(i = m = 1, \ldots, 5)$. The upper bounds for complete inseparability are slightly different from the usual ones because of the use of normalized nullifiers [7,19].

(a) Linear:

$$\bar{\delta}_1 = \frac{y_1(\theta_1) - x_2(\theta_2)}{\sqrt{2}},$$
$$\bar{\delta}_2 = \frac{y_2(\theta_2) - x_1(\theta_1) - x_3(\theta_3)}{\sqrt{3}},$$
$$\bar{\delta}_3 = \frac{y_3(\theta_3) - x_2(\theta_2) - x_4(\theta_4)}{\sqrt{3}},$$
$$\bar{\delta}_4 = \frac{y_4(\theta_4) - x_3(\theta_3) - x_5(\theta_5)}{\sqrt{3}},$$
$$\bar{\delta}_5 = \frac{y_5(\theta_5) - x_4(\theta_4)}{\sqrt{2}},$$
$$V(\bar{\delta}_i) + V(\bar{\delta}_{i+1}) \geq \begin{cases} \sqrt{\frac{8}{3}} & \text{for i=1, N-1,} \\ \frac{4}{3} & \text{for i=2, \ldots, N-2.} \end{cases}$$

(b) Pentagon:

$$\bar{\delta}_i = \frac{y_i(\theta_i) - [x_{i+1}(\theta_{i+1}) + x_{i-1}(\theta_{i-1})]}{\sqrt{3}},$$
$$V(\bar{\delta}_i) + V(\bar{\delta}_{i+1}) \geq \tfrac{4}{3} \quad \text{for } i = 1, \ldots, 4,$$

with $x_0(\theta_0) \equiv x_5(\theta_5)$ and $x_6(\theta_6) \equiv x_1(\theta_1)$.

(c) Star:

$$\bar{\delta}_i = \frac{y_i(\theta_i) - x_3(\theta_3)}{\sqrt{2}} \quad \text{for } i \neq 3,$$
$$\bar{\delta}_3 = \frac{y_3(\theta_3) - \sum_{i\neq 3}^{5} x_i(\theta_i)}{\sqrt{5}},$$
$$V(\bar{\delta}_i) + V(\bar{\delta}_3) \geq \sqrt{\frac{8}{5}} \quad \text{for } i \neq 3.$$

TABLE III. Nonlinear supermode basis-based cluster-state generation in a five-waveguides ANWs with homogeneous coupling profile for the linear, pentagon, star, square pyramid, and GHZ graphs. We show the value of the nullifiers $[V(\bar{\delta}_i)]$, pump-power profile $\vec{\eta}$, pump phase profile $\vec{\phi}$, and local oscillator phase profile $\vec{\theta}$. The matrices $\bar{\mathcal{O}}$ and $\bar{\mathcal{O}}_{\text{post}}$ obtained for each case are shown in Appendix B. Simultaneous values of $V(\bar{\delta}_i)$ under the shot noise threshold $V(\bar{\delta}_i) = 1$ are a signature of successful cluster generation. Here $C_0 = 0.24\ \text{mm}^{-1}$ and $z = 30$ mm.

Graph	Nullifiers $[V(\bar{\delta}_i)]$	$\vec{\eta} \times 10^2\ \text{mm}^{-1}$	$\vec{\phi}/\pi$	$\vec{\theta}/\pi$
Linear	$\{0.29, 0.36, 0.45, 0.13, 0.09\}$	$\{4.1, 1.8, 3.6, 1.3, 1.0\}$	$\{0.78, -0.59, -0.26, 0.34, -0.97\}$	$\{-1.09, -0.09, 0.37, 1.37, 0.24\}$
Pentagon	$\{0.28, 0.25, 0.31, 0.17, 0.32\}$	$\{0.7, 2.5, 3.3, 3.4, 1.4\}$	$\{-0.01, -1.41, -0.40, -0.16, 0.26\}$	$\{$-0.47, -2.57, -0.32, 2.15, 0.72$\}$
Star	$\{0.30, 0.28, 0.35, 0.43, 0.20\}$	$\{3.2, 0.5, 0.9, 0.5, 1.7\}$	$\{-0.02, 0.75, -0.34, -0.54, 0.04\}$	$\{-0.24, -0.08, 0.15, 0.28, -0.23\}$
Pyramid	$\{0.47, 0.38, 0.19, 0.41, 0.26\}$	$\{1.3, 0.4, 3.5, 1.7, 3.3\}$	$\{1.21, 1.01, -0.09, 1.60, -0.08\}$	$\{0.26, -1.01, -0.09, -0.68, 0.53\}$
GHZ	$\{0.48, 0.31, 0.38, 0.23, 0.24\}$	$\{4.0, 1.5, 2.8, 2.4, 4.3\}$	$\{0.13, -0.04, -0.08, -0.04, -0.04\}$	$\{0.56, 0.07, 0.24, 0.08, -0.44\}$

(d) Square pyramid:

$$\bar{\delta}_1 = \frac{y_1(\theta_1) - [x_2(\theta_2) + x_3(\theta_3) + x_5(\theta_5)]}{2},$$

$$\bar{\delta}_2 = \frac{y_2(\theta_2) - [x_1(\theta_1) + x_3(\theta_3) + x_4(\theta_4)]}{2},$$

$$\bar{\delta}_3 = \frac{y_3(\theta_3) - \sum_{i\neq 3}^{5} x_i(\theta_i)}{\sqrt{5}},$$

$$\bar{\delta}_4 = \frac{y_4(\theta_4) - y_1(\theta_1)}{\sqrt{2}},$$

$$\bar{\delta}_5 = \frac{y_5(\theta_5) - y_2(\theta_2)}{\sqrt{2}},$$

$$V(\bar{\delta}_i) + V(\bar{\delta}_3) \geq \sqrt{\frac{8}{5}} \quad \text{for } i = 4, 5.$$

Here we have used the fact that linear combinations of nullifiers are also nullifiers in order to define $\bar{\delta}_{4,5}$. Because of the symmetry of the cluster, the four VLF inequalities are degenerate two by two.

(e) The GHZ cluster state is equivalent to the star cluster by means of a $\pi/2$ LO rotation for all modes $i \neq 3$, as demonstrated in Ref. [67]. Applying this labeling we obtain

$$\bar{\delta}_i = \frac{x_i(\theta_i) - x_3(\theta_3)}{\sqrt{2}} \quad \text{for } i \neq 3,$$

$$\bar{\delta}_3 = \frac{\sum_{i=1}^{5} y_i(\theta_i)}{\sqrt{5}},$$

$$V(\bar{\delta}_i) + V(\bar{\delta}_3) \geq \sqrt{\frac{8}{5}} \quad \text{for } i \neq 3.$$

Thus, a GHZ cluster state is generated using the same set of parameters as that obtained for the star cluster with a $\pi/2$ LO rotation in all the modes except mode 3.

APPENDIX B

In this appendix we derive Eq. (13), introduce some definitions used in Sec. V, and show an example of emulation of the statistics associated with the five-node linear cluster state of Fig. 5 using nonlinear supermodes.

The transformation S_C is a symplectic and orthogonal transformation that produces the cluster Eq. (11) from N-phase $(\hat{y})$-squeezed input states given by a diagonal matrix with positive entries $\bar{K}^2(\vec{r})$. The cluster thus has an associated covariance matrix $V_C = S_C \bar{K}^2(\vec{r})\, S_C^{\top}$. A symmetric cluster transformation S_C can be obtained from the adjacency matrix J as [66]

$$S_C = \begin{pmatrix} X_s & -Y_s \\ Y_s & X_s \end{pmatrix}$$

with $X_s = (J^2 + I)^{-1/2}$, $Y_s = JX_s$, and I the identity matrix. The transformation related to the cluster shape S_C is defined up to a transformation $\bar{S}_C(\vec{\varphi}) = S_C\,\bar{\mathcal{O}}(\vec{\varphi})$, where $\bar{\mathcal{O}}(\vec{\varphi}) = [\mathcal{O}(\vec{\varphi}), \mathcal{O}(\vec{\varphi})]$ and $\mathcal{O}(\vec{\varphi})$ is an N-dimensional orthogonal matrix. This degree of freedom is related to the freedom of distributing the degree of squeezing among the cluster modes $\tilde{K}^2(\vec{r}, \vec{\varphi}) = \bar{\mathcal{O}}(\vec{\varphi})\bar{K}^2(\vec{r})\bar{\mathcal{O}}(\vec{\varphi})^\top$. Thus, setting the nonlinear supermodes as the basis, the cluster is built from, i.e., taking $K^2(\vec{\eta}, \vec{\phi}, z) = \bar{K}^2(\vec{r})$, the cluster V_C and the ANWs $V(z)$ covariance matrices are related through Eq. (8) by

$$V_C = S_{\mathrm{LO}}(\vec{\eta}, \vec{\phi}, \vec{\varphi}, z)V(z)S_{\mathrm{LO}}^\top(\vec{\eta}, \vec{\phi}, \vec{\varphi}, z),$$

where $S_{\mathrm{LO}}(\vec{\eta}, \vec{\phi}, \vec{\varphi}, z) = S_C\bar{\mathcal{O}}(\vec{\varphi})R_1^\top(\vec{\eta}, \vec{\phi}, z)$. Note that we have used $K^2(z) \equiv K^2(\vec{\eta}, \vec{\phi}, z)$ and $R_1(z) \equiv R_1(\vec{\eta}, \vec{\phi}, z)$ in order to emphasize the dependence of the Bloch-Messiah decomposition with the pump parameters.

The postprocessing matrix $\bar{\mathcal{O}}_{\mathrm{post}}(\vartheta)$ is an orthogonal matrix given by $\bar{\mathcal{O}}_{\mathrm{post}}(\vartheta) = [\mathcal{O}_{\mathrm{post}}(\vartheta), \mathcal{O}_{\mathrm{post}}(\vartheta)]$. Both matrices $\mathcal{O}(\varphi)$ and $\bar{\mathcal{O}}_{\mathrm{post}}(\vartheta)$ can be decomposed into $N(N-1)/2$ rotation matrices parametrized for instance by generalized Euler angles [87]. In our simulations of the five-node cluster states we use ten generalized Euler angles to parametrized each matrix: $\vec{\varphi} = (\varphi_1, \ldots, \varphi_{10})$, $\vec{\vartheta} = (\vartheta_1, \ldots, \vartheta_{10})$. These matrices take into account all possible rotations in a five-dimensional space.

The matrix $D_{\mathrm{LO}}(\vec{\theta})$ is related to the LO phase profile $\vec{\theta}$, written as

$$D_{\mathrm{LO}}(\vec{\theta}) = \begin{pmatrix} \cos(\vec{\theta}) & \sin(\vec{\theta}) \\ -\sin(\vec{\theta}) & \cos(\vec{\theta}) \end{pmatrix},$$

where $\cos(\vec{\theta}) = [\cos(\theta_1), \ldots, \cos(\theta_j), \ldots, \cos(\theta_N)]$ with $\sin(\vec{\theta})$ defined similarly. We have used five local oscillator phases $\vec{\theta} = (\theta_1, \ldots, \theta_5)$ in our simulations.

We show an example of method (ii) introduced in Sec. V B with the cluster states of Fig. 5. The nodes of a given graph are obtained by applying the corresponding transformations $\bar{S}_C(\vec{\varphi})$ to the nonlinear supermodes. We choose to minimize the following fitness function with 35 free parameters: $F_P(\vec{\eta}, \vec{\phi}, \vec{\varphi}, \vec{\theta}, \vec{\vartheta}) = \|S_{\mathrm{LO}}(\vec{\eta}, \vec{\phi}, \vec{\varphi}, z) - \bar{O}_{\mathrm{post}}(\vec{\vartheta})D_{\mathrm{LO}}(\vec{\theta})\|$. Here we use the Frobenius norm $\|A\|^2 = \sum_{i,j} |A_{i,j}|^2$. The optimization of this function produces a quantum state characterized by $V(z)$, which after BHD in adequate individual quadratures and postprocessing of electrical gains is fully equivalent to a given cluster state characterized by V_C. In Table III we list the optimized nullifier variances obtained for the $N = 5$ node cluster states shown in Fig. 5. We use the same working point as for Table I: homogeneous coupling profile $f_j = 1$ with coupling strength $C_0 = 0.24\ \mathrm{mm}^{-1}$ and a fixed length $z = 30$ mm. Remarkably, we again find a realistic set of pump and LO parameters $\{\vec{\eta}, \vec{\phi}, \vec{\theta}\}$ where the clusters are generated in the five analyzed cases. The nullifiers thus produced also violate the inseparability conditions shown in Appendix A.

The parameters $(\vec{\eta}, \vec{\phi}, \vec{\theta})$ optimized for each cluster are displayed in Table III. We show below as an example the matrices X_s, Y_s, $\mathcal{O}$, and $\mathcal{O}_{\mathrm{post}}$ used to optimize the generation of the linear cluster. Similar values are obtained for the other clusters shown in Table III.

$$X_s = \begin{pmatrix} \frac{(3\sqrt{2}+5)}{12} & 0 & -\frac{1}{6} & 0 & \frac{(5-3\sqrt{2})}{12} \\ 0 & \frac{(\sqrt{2}+1)}{4} & 0 & \frac{(1-\sqrt{2})}{4} & 0 \\ -\frac{1}{6} & 0 & \frac{2}{3} & 0 & -\frac{1}{6} \\ 0 & \frac{(1-\sqrt{2})}{4} & 0 & \frac{(\sqrt{2}+1)}{4} & 0 \\ \frac{(5-3\sqrt{2})}{12} & 0 & -\frac{1}{6} & 0 & \frac{(3\sqrt{2}+5)}{12} \end{pmatrix},$$

$$Y_s = \begin{pmatrix} 0 & \frac{(\sqrt{2}+1)}{4} & 0 & \frac{(1-\sqrt{2})}{4} & 0 \\ \frac{(\sqrt{2}+1)}{4} & 0 & \frac{1}{2} & 0 & \frac{(1-\sqrt{2})}{4} \\ 0 & \frac{1}{2} & 0 & \frac{1}{2} & 0 \\ \frac{(1-\sqrt{2})}{4} & 0 & \frac{1}{2} & 0 & \frac{(\sqrt{2}+1)}{4} \\ 0 & \frac{(1-\sqrt{2})}{4} & 0 & \frac{(\sqrt{2}+1)}{4} & 0 \end{pmatrix},$$

$$\mathcal{O} = \begin{pmatrix} -0.03 & -0.61 & -0.62 & 0.40 & 0.29 \\ 0.02 & 0.28 & -0.38 & -0.63 & 0.62 \\ 0.01 & 0.21 & 0.45 & 0.51 & 0.70 \\ 0.32 & 0.67 & -0.49 & 0.41 & -0.19 \\ -0.95 & 0.25 & -0.14 & 0.12 & -0.06 \end{pmatrix},$$

$$\mathcal{O}_{\mathrm{post}} = \begin{pmatrix} 0.11 & 0.62 & -0.62 & -0.29 & 0.36 \\ 0.07 & -0.14 & -0.62 & 0.71 & -0.28 \\ 0.73 & -0.18 & -0.14 & -0.42 & -0.49 \\ -0.60 & -0.42 & -0.43 & -0.48 & -0.20 \\ 0.30 & -0.62 & -0.15 & 0.00(4) & 0.71 \end{pmatrix}.$$

[1] A. Acín, I. Bloch, H. Buhrman, T. Calarco, C. H. Eichler, J. Eisert, D. Esteve, N. Gisin, S. J. Glaser, F. Jelezko, S. Kuhr, M. Lewenstein, M. F. Riedel, P. O. Schmidt, R. Thew, A. Wallraff, I. Walmsley, and F. K. Wilhelm, The quantum technologies roadmap: A European community view, New J. Phys. **20**, 080201 (2018).

[2] M. D. Reid, P. D. Drummond, W. P. Bowen, E. G. Cavalcanti, P. K. Lam, H. A. Bachor, U. L. Andersen, and G. Leuchs, Colloquium: The Einstein-Podolsky-Rosen paradox: From concepts to applications, Rev. Mod. Phys. **81**, 1727 (2009).

[3] A. Furusawa, *Quantum States of Light* (Springer, Tokio, 2015).

[4] S. L. Braunstein and P. van Loock, Quantum information with continuous variables, Rev. Mod. Phys. **77**, 513 (2005).

[5] R. Raussendorf and H. J. Briegel, A One-Way Quantum Computer, Phys. Rev. Lett. **86**, 5188 (2001).

[6] N. C. Menicucci, P. van Loock, M. Gu, C. Weedbrook, T. C. Ralph, and M. A. Nielsen, Universal Quantum Computation with Continuous-Variable Cluster States, Phys. Rev. Lett. **97**, 110501 (2006).

[7] M. V. Larsen, X. Guo, C. R. Breum, J. S. Neergaard-Nielsen, and U. L. Andersen, Deterministic generation of a two-dimensional cluster state, Science **366**, 369 (2019).

[8] W. Asavanant, Y. Shiozawa, S. Yokoyama, B. Charoensombutamon, H. Emura, R. N. Alexander, S. Takeda, J. Yoshikawa, N. C. Menicucci, H. Yonezawa, and A. Furusawa, Generation of time-domain-multiplexed two-dimensional cluster state, Science **366**, 373 (2019).

[9] M. Chen, N. C. Menicucci, and O. Pfister, Experimental Realization of Multipartite Entanglement of 60 Modes of a Quantum Optical Frequency Comb, Phys. Rev. Lett. **112**, 120505 (2014).

[10] J.-I. Yoshikawa, S. Yokoyama, T. Kaji, Ch. Sornphiphatphong, Y. Shiozawa, K. Makino, and A. Furusawa, Generation of one-million-mode continuous-variable cluster state by unlimited time-domain multiplexing, APL Photonics **1**, 060801 (2016).

[11] M. Yukawa, R. Ukai, P. van Loock, and A. Furusawa, Experimental generation of four-mode continuous-variable cluster states, Phys. Rev. A **78**, 012301 (2008).

[12] X. Su, S. Hao, X. Deng, L. Ma, M. Wang, X. Jia, C. Xie, and K. Peng, Gate sequence for continuous variable one-way quantum computation, Nat. Commun. **4**, 2828 (2013).

[13] S. Armstrong, M. Wang, R. Y. Teh, Q. Gong, Q. He, J. Janousek, H.-A. Bachor, M. D. Reid, and P. K. Lam, Multipartite Einstein-Podolsky-Rosen steering and genuine tripartite entanglement with optical networks, Nat. Phys. **11**, 167 (2015).

[14] J. Nokkala, F. Arzani, F. Galve, R. Zambrini, S. Maniscalco, J. Piilo, N. Treps, and V. Parigi, Reconfigurable optical implementation of quantum complex networks, New J. Phys. **20**, 053024 (2018).

[15] N. Killoran, T. B. Bromley, J. M. Arrazola, M. Schuld, N. Quesada, and S. Lloyd, Continuous-variable quantum neural networks, Phys. Rev. Res. **1**, 033063 (2019).

[16] S. Armstrong, J.-F. Morizur, J. Janousek, B. Hage, N. Treps, P. K. Lam, and H.-A. Bachor, Programmable multimode quantum networks, Nat. Commun. **3**, 1026 (2012).

[17] J. Roslund, R. Medeiros de Araujo, S. Jiang, C. Fabre, and N. Treps, Wavelength-multiplexed quantum networks with ultrafast frequency combs, Nat. Photonics **8**, 109 (2014).

[18] Y. Cai, J. Roslund, G. Ferrini, F. Arzani, X. Xu, C. Fabre, and N. Treps, Multimode entanglement in reconfigurable graph states using optical frequency combs, Nat. Commun. **8**, 15645 (2017).

[19] S. Takeda, K. Takase, and A. Furusawa, On-demand photonic entanglement synthesizer, Sci. Adv. **5**, eaaw4530 (2019).

[20] M. Hillery, V. Buzek, and A. Berthiaume, Quantum secret sharing, Phys. Rev. A **59**, 1829 (1999).

[21] X. Guo, C. R. Breum, J. Borregaard, S. Izumi, M. V. Larsen, T. Gehring, M. Christlandl, J. S. Neergaard-Nielsen, and U. L. Andersen, Distributed quantum sensing in a continuous variable entangled network, Nat. Phys. **16**, 281 (2020).

[22] J. Wang, F. Sciarrino, A. Laing, and M. G. Thompson, Integrated photonic quantum technologies, Nat. Photonics **14**, 273 (2020).

[23] F. Lenzini, J. Janousek, O. Thearle, M. Villa, B. Haylock, S. Kasture, L. Cui, H.-P. Phan, D. V. Dao, H. Yonezawa, P. K. Lam, E. H. Huntington, and M. Lobino, Integrated photonic platform for quantum information with continuous variables, Sci. Adv. **4**, eaat9331 (2018).

[24] R. Kruse, F. Katzschmann, A. Christ, A. Schreiber, S. Wilhelm, K. Laiho, A. Gábris, C. S. Hamilton, I. Jex, and Ch. Silberhorn, Spatio-spectral characteristics of parametric down-conversion in waveguide arrays, New J. Phys. **15**, 083046 (2013).

[25] A. S. Solntsev, F. Setzpfandt, A. S. Clark, C. W. Wu, M. J. Collins, C. Xiong, A. Schreiber, F. Katzschmann, F. Eilenberger, R. Schieck, W. Sohler, A. Mitchell, Ch. Silberhorn, B. J. Eggleton, T. Pertsch, A. A. Sukhourukov, D. N. Neshev, and Y. S. Kivshar, Generation of Nonclassical Biphoton States through Cascaded Quantum Walks on a Nonlinear Chip, Phys. Rev. X **4**, 031007 (2014).

[26] J. C. Adcock, C. Vigliar, R. Santagati, J. W. Silverstone, and M. G. Thompson, Programmable four-photon graph states on a silicon chip, Nat. Commun. **10**, 3528 (2019).

[27] J. G. Titchener, A. S. Solntsev, and A. A. Sukhorukov, Reconfigurable cluster-state generation in specially poled nonlinear waveguide arrays, Phys. Rev. A **101**, 023809 (2020).

[28] A. Rai and D. G. Angelakis, Dynamics of nonclassical light in integrated nonlinear waveguide arrays and generation of robust continuous-variable entanglement, Phys. Rev. A **85**, 052330 (2012).

[29] D. Barral, K. Bencheikh, N. Belabas, and J. A. Levenson, Zero supermode-based multipartite entanglement in $\chi^{(2)}$ nonlinear waveguide arrays, Phys. Rev. A **99**, 051801(R) (2019).

[30] O. Alibart, V. D'Auria, M. De Micheli, F. Doutre, F. Kaiser, L. Labonté, T. Lunghi, E. Picholle, and S. Tanzilli, Quantum photonics at telecom wavelengths based on lithium niobate waveguides, J. Opt. **18**, 104001 (2016).

[31] J. Liñares, M. C. Nistal, and D. Barral, Quantization of coupled 1D vector modes in integrated photonic waveguides, New J. Phys. **10**, 063023 (2008).

[32] J. M. Moison, N. Belabas, C. Minot, and J. A. Levenson, Discrete photonics in waveguide arrays, Opt. Lett. **34**, 2462 (2009).

[33] R. J. Chapman, M. Santandrea, Z. Huang, G. Corrielli, A. Crespi, M.-H. Yung, R. Osellame, and A. Peruzzo, Experimental perfect state transfer of an entangled photonic qubit, Nat. Commun. **7**, 11339 (2016).

[34] S. Weimann, A. Perez-Leija, M. Lebugle, R. Keil, M. Tichy, M. Grafe, R. Heilmann, S. Nolte, H. Moya-Cessa, G. Weihs, D. N. Christodoulides, and A. Szameit, Implementation of quantum and classical discrete fractional Fourier transforms, Nat. Commun. **7**, 11027 (2016).

[35] A. Blanco-Redondo, B. Bell, D. Oren, B. J. Eggleton, and M. Segev, Topological protection of biphoton states, Science **362**, 568 (2018).

[36] D. S. Hum and M. M. Fejer, Quasi-phasematching, C.R. Physique **8**, 180 (2007).

[37] D. Barral, N. Belabas, K. Bencheikh, and J. A. Levenson, Coupling quasi-phase-matching: Entanglement buildup in

$\chi^{(2)}$ nonlinear-waveguide arrays, Phys. Rev. A **100**, 013824 (2019).

[38] R. Iwanow, R. Schieck, G. I. Stegeman, T. Pertsch, F. Lederer, Y. Min, and W. Sohler, Observation of Discrete Quadratic Solitons, Phys. Rev. Lett. **93**, 113902 (2004).

[39] E. Kapon, J. Katz, and A. Yariv, Supermode analysis of phase-locked arrays of semiconductor lasers, Opt. Lett. **10**, 125 (1984).

[40] G. Patera, N. Treps, C. Fabre, and G. J. Valcarcel, Quantum theory of synchronously pumped type I optical parametric oscillators: Characterization of the squeezed supermodes, Eur. Phys. J. D **56**, 123 (2010).

[41] C. Fabre and N. Treps, Modes and states in quantum optics, Rev. Mod. Phys. **92**, 35005 (2020).

[42] N. K. Efremidis and D. N. Christodoulides, Revivals in engineered waveguide arrays, Opt. Commun. **246**, 345 (2005).

[43] E.-O. Bossé and L. Vinet, Coherent transport in photonic lattices: A survey of recent analytic results, SIGMA **13**, 074 (2017).

[44] F. Arzani, C. Fabre, and N. Treps, Versatile engineering of multimode squeezed states by optimizing the pump spectral profile in spontaneous parametric down-conversion, Phys. Rev. A **97**, 033808 (2018).

[45] D. Barral, M. Walschaers, K. Bencheikh, V. Parigi, J. A. Levenson, N. Treps, and N. Belabas, Quantum State Engineering in Arrays of Nonlinear Waveguides, Phys. Rev. A (to be published).

[46] A. Christ, B. Brecht, W. Mauerer, and Ch. Silberhorn, Theory of quantum frequency conversion and type-II parametric down-conversion in the high-gain regime, New J. Phys. **15**, 043038 (2013).

[47] J. Fiurasek and J. Perina, Substituting scheme for nonlinear couplers: A group approach, Phys. Rev. A **62**, 033808 (2000).

[48] N. Quesada and J. E. Sipe, Effects of time ordering in quantum nonlinear optics, Phys. Rev. A **90**, 063840 (2014).

[49] G. Cariolaro and G. Pierobon, Bloch-Messiah reduction of Gaussian unitaries by Takagi factorization, Phys. Rev. A **94**, 062109 (2016).

[50] C. S. Hamilton, R. Kruse, L. Sansoni, Ch. Silberhorn, and I. Jex, Driven Quantum Walks, Phys. Rev. Lett. **113**, 083602 (2014).

[51] G. Adesso, S. Ragy, and A. R. Lee, Continuous variable quantum information: Gaussian states and beyond, Open Syst. Inf. Dyn. **21**, 1440001 (2014).

[52] S. L. Braunstein, Squeezing as an irreducible resource, Phys. Rev. A **71**, 055801 (2005).

[53] F. Kaiser, B. Fedrici, A. Zavatta, V. D'Auria, and S. Tanzilli, A fully guided-wave squeezing experiment for fiber quantum networks, Optica **3**, 362 (2016).

[54] M. G. Raymer, D. F. McAlister, and U. Leonhardt, Two-mode quantum-optical state measurement: Sampling the joint density matrix, Phys. Rev. A **54**, 2397 (1996).

[55] V. D'Auria, S. Fornaro, A. Porzio, S. Solimeno, S. Olivares, and M. G. A. Paris, Full Characterization of Gaussian Bipartite Entangled States by a Single Homodyne Detector, Phys. Rev. Lett. **102**, 020502 (2009).

[56] D. Barral, N. Belabas, L. M. Procopio, V. D'Auria, S. Tanzilli, and J. A. Levenson, Continuous-variable entanglement of two bright coherent states that never interacted, Phys. Rev. A **96**, 053822 (2017).

[57] B. R. Mollow and R. J, Glauber: Quantum theory of parametric amplification I, Phys. Rev. **160**, 1076 (1967).

[58] D. Barral, K. Bencheikh, J. A. Levenson, and N. Belabas, How to create entanglement among 100 spatial modes with a single photonic lattice, arXiv:2005.07241 (2020).

[59] The generalized amplitude and phase quadratures in a given basis with index i are respectively defined as $x_i(\theta_i) = x_i\cos(\theta_i) + y_i\sin(\theta_i)$ and $y_i(\theta_i) = -x_i\sin(\theta_i) + y_i\cos(\theta_i)$.

[60] M. Epping, H. Kampermann, Ch. Macchiavello, and D. Bruss, Multi-partite entanglement can speed up quantum key distribution in networks, New J. Phys. **19**, 093012 (2017).

[61] Y. Hasegawa, R. Ikuta, N. Matsuda, K. Tamaki, H.-K. Lo, T. Yamamoto, K. Azuma, and N. Imoto, Experimental time-reversed adaptative Bell measurement towards all-photonic quantum repeaters, Nat. Commun. **10**, 378 (2019).

[62] P. van Loock and A. Furusawa, Detecting genuine multipartite continuous-variable entanglement, Phys. Rev. A **67**, 052315 (2003).

[63] $V\sum_i l_i\xi_i \equiv \sum_i l_i^2 V(\xi_i,\xi_i) + \sum_{i\neq i'} l_i l_i' V(\xi_i,\xi_i')$ with l_i a set of real numbers.

[64] H.-G. Beyer and H.-P. Schwefel, Evolution strategies: A comprehensive introduction, Nat. Comput. **1**, 3 (2002).

[65] M. Gu, C. Weedbrook, N. C. Menicucci, T. C. Ralph, and P. van Loock, Quantum computing with continuous-variable clusters, Phys. Rev. A **79**, 062318 (2009).

[66] G. Ferrini, J. P. Gazeau, T. Coudreau, C. Fabre, and N. Treps, Compact Gaussian quantum computation by multi-pixel homodyne detection, New J. Phys. **15**, 093015 (2013).

[67] N. C. Menicucci, S. T. Flammia, H. Zaidi, and O. Pfister, Ultracompact generation of continuous-variable cluster states, Phys. Rev. A **76**, 010302(R) (2007).

[68] G. Ferrini, J. Roslund, F. Arzani, C. Fabre, and N. Treps, Direct approach to Gaussian measurement based quantum computation, Phys. Rev. A **94**, 062332 (2016).

[69] Since a network usually refers to distributable nodes, we follow [18] and talk about a quantum graph in nonlinear supermode-based bases.

[70] R. Ukai, J.-I. Yoshikawa, N. Iwata, P. van Loock, and A. Furusawa, Universal linear Bogoliubov transformations through one-way quantum computation, Phys. Rev. A **81**, 032315 (2010).

[71] M. Christandl and S. Wehner, in *Proceedings of ASIACRYPT 2005*, Lecture Notes in Computer Science Vol. 3788 (Springer, Berlin, 2005), p. 217.

[72] N. C. Menicucci, B. Q. Baragiola, T. F. Demarie, and G. K. Brennen, Anonymous broadcasting of classical information with a continuous-variable topological quantum code, Phys. Rev. A **97**, 032345 (2018).

[73] N. C. Menicucci, Fault-Tolerant Measurement-Based Quantum Computing with Continuous-Variable Cluster States, Phys. Rev. Lett. **112**, 120504 (2014).

[74] K. Fukui, A. Tomita, A. Okamoko, and K. Fuji, High-Threshold Fault-Tolerant Quantum Computation with Analog Quantum Error Correction, Phys. Rev. X **8**, 021054 (2018).

[75] O. Pfister, Continuous-variable quantum computing in the quantum optical frequency comb, J. Phys. B **53**, 012001 (2019).

[76] D. Barral, D. Balado, and J. Liñares, Generation and detection of continuous variable quantum vortex states via compact photonic devices, Photonics **4**, 2 (2017).

[77] M. Walschaers, S. Sarkar, V. Parigi, and N. Treps, Tailoring Non-Gaussian Continuous-Variable Graph States, Phys. Rev. Lett. **121**, 220501 (2018).

[78] C. S. Hamilton, R. Kruse, L. Sansoni, S. Barkhofen, Ch. Silberhorn, and I. Jex, Gaussian Boson Sampling, Phys. Rev. Lett. **119**, 170501 (2017).

[79] J. Huh, G. G. Guerreschi, B. Peropadre, J. R. McClean, and A. Aspuru-Guzik, Boson sampling for molecular vibronic spectra, Nat. Phys. **9**, 615 (2015).

[80] W. R. Clements, J. J. Renema, A. Eckstein, A. A. Valido, A. Lita, T. Gerrits, S. W. Nam, W. S. Kolthammer, J. Huh, and I. A. Walmsley, Approximating vibronic spectroscopy with imperfect quantum optics, J. Phys. B: At. Mol. Opt. Phys. **51**, 245503 (2018).

[81] S. Paesani, Y. Ding, R. Santagati, L. Chakhmakhchyan, C. Vigliar, K. Rottwitt, L. K. Oxenlowe, J. Wang, M. G. Thompson, and A. Laing, Generation and sampling of quantum states of light in a silicon chip, Nat. Phys. **15**, 925 (2019).

[82] H. Jin, F. M. Liu, P. Xu, J. L. Xia, M. L. Zhong, Y. Yuan, J. W. Zhou, Y. X. Gong, W. Wang, and S. N. Zhu, On-Chip Generation and Manipulation of Entangled Photons Based on Reconfigurable Lithium-Niobate Waveguide Circuits, Phys. Rev. Lett. **113**, 103601 (2014).

[83] F. Mondain, T. Lunghi, A. Zavatta, E. Gouzien, F. Doutre, M. De Micheli, S. Tanzilli, and V. D'Auria, Chip-based squeezing at a telecom wavelength, Photon. Res. **7**, A36 (2019).

[84] A. Boes, B. Corcoran, L. Chang, J. Bowers, and A. Mitchell, Status and potential of Lithium Niobate on Insulator (LNOI) for photonic integrated circuits, Laser Photon. Rev. **12**, 1700256 (2018).

[85] Ch. Wang, C. Langrock, A. Marandi, M. Jankowski, M. Zhang, B. Desiatov, M. M. Fejer, and M. Loncar, Ultrahigh-efficiency wavelength conversion in nanophotonic periodically poled lithium niobate waveguides, Optica **5**, 1438 (2018).

[86] T. Kashiwazaki, N. Takanashi, T. Yamashima, T. Kazama, K. Enbutsu, R. Kasahara, T. Umeki, and A. Furusawa, Continuous-wave 6-dB-squeezed light with 2.5-THz-bandwidth from single-mode PPLN waveguide, APL Photonics **5**, 036104 (2020).

[87] G. B. Arfken and H. J. Weber, *Mathematical Methods for Physicists* (Elsevier, 2005).